

## RESEARCH LETTER

10.1029/2018GL080470

### Key Points:

- Effective stress principle only applies if fluid pressure is homogeneous
- High injection rate and high stresses enhance in-plane fluid pressure heterogeneity
- At high injection rate, high localized fluid overpressure is required for fault reactivation

### Correspondence to:

F. X. Passelègue,  
passelegue@gmail.com

### Citation:

Passelègue, F. X., Brantut, N., & Mitchell, T. M. (2018). Fault reactivation by fluid injection: Controls from stress state and injection rate. *Geophysical Research Letters*, 45, 12,837–12,846. <https://doi.org/10.1029/2018GL080470>

Received 13 SEP 2018

Accepted 1 DEC 2018

Accepted article online 5 DEC 2018

Published online 13 DEC 2018

## Fault Reactivation by Fluid Injection: Controls From Stress State and Injection Rate

François X. Passelègue<sup>1</sup> , Nicolas Brantut<sup>2</sup> , and Thomas M. Mitchell<sup>2</sup> 

<sup>1</sup>Mécanique des Roches, École Polytechnique Fédérale de Lausanne, Lausanne, Switzerland, <sup>2</sup>Department of Earth Sciences, University College London, London, UK

**Abstract** We studied the influence of stress state and fluid injection rate on the reactivation of faults. We conducted experiments on a saw cut Westerly granite sample under triaxial stress conditions. Fault reactivation was triggered by injecting fluids through a borehole directly connected to the fault. Our results show that the peak fluid pressure at the borehole leading to reactivation increases with injection rate. Elastic wave velocity measurements along-fault strike highlight that high injection rates induce significant fluid pressure heterogeneities, which explains that in such cases, the onset of fault reactivation is not determined by a conventional Coulomb law and effective stress principle, but rather by a nonlocal rupture initiation criterion. Our results demonstrate that increasing the injection rate enhances the transition from drained to locally undrained conditions, where local but intense fluid pressures perturbations can reactivate large faults, and contribute to continuing seismicity beyond the period of injection.

**Plain Language Summary** One of the most worrisome picture of the recent years in geophysics corresponds to the exponential increase of the seismicity in Oklahoma since the beginning of deep wastewater injections. In order to reduce seismic hazard, regulators have planned a 40% reduction in the injection volume per day. While the reactivation of fault due to fluid pressure has been extensively studied, the influence of injection rate on fault reactivation remains poorly documented. In this study, we present state of the art experimental results regarding the influence of the state of stress and of the injection rate on the onset of fault reactivation. Our results demonstrate that an increase of the stress acting on the fault and/or of the injection rate induce the transition from a drained system where the classical reactivation theory is respected, toward an undrained system where the onset of fault reactivation is not determined by conventional Coulomb law and effective stress principle. Our results suggest that in such conditions, the reactivation of fault is a function of the size of the fault patch affected by the fluid pressure, that is, the diffusion of the fluid along the fault, rather than a function of the initial state of stress.

### 1. Introduction

In the last decade, exploitation of geothermal and hydrocarbon reservoirs (Cornet et al., 1997; Warpinski & Teufel, 1987), as well as deep fluid injection for geological storage (Healy et al., 1968; Raleigh et al., 1976; Zoback & Harjes, 1997), induced a strong increase in seismicity (Ellsworth, 2013). One of the strongest evidence for injection-induced or triggered seismicity is the recent rise in the earthquake rate in Oklahoma that occurred since the beginning of deep wastewater injection associated with unconventional oil reservoir exploitation (Ellsworth, 2013). This induced seismicity includes earthquakes of magnitude larger than 5 that have caused significant damage (Keranen et al., 2013; Rubinstein et al., 2014). The recent Pawnee  $M_w=5.8$  earthquake was the largest in instrumented history in Oklahoma and is only slightly below the maximum magnitude expected during 1,900 years of tectonic activity (Langenbruch & Zoback, 2016). In order to reduce seismic hazard, Oklahoma regulators applied a 40% reduction in the injection volume per day. This reduction of the injection rate sensibly decreased the seismicity in Oklahoma in the past three years, suggesting that injection rate controls the intensity of induced and triggered seismicity. However, the influence of injection rate on fault reactivation and induced seismicity remains poorly documented and intensively discussed (Barbour et al., 2017; Dieterich et al., 2015; Goebel et al., 2017; Langenbruch & Zoback, 2016).

From a physical point of view, our understanding of the mechanics of fault reactivation and earthquake nucleation due to fluid pressure variations is based on the concept of effective stress combined with a Coulomb

failure criterion. The onset of fault reactivation is typically characterized by a critical shear stress  $\tau_p$  given by the product of a friction coefficient  $\mu$  (ranging from 0.6 to 0.85 in most crustal rock types; see Byerlee, 1978), and the normal stress  $\sigma$  applied on the fault. In the presence of fluids, this normal stress is offset by an amount equal to the fluid pressure  $p$ , so that the fault reactivation criterion is (Jaeger et al., 2009; Sibson, 1985)

$$\tau \geq \tau_p = \mu(\sigma - p). \quad (1)$$

This simple concept has been used extensively to explain a range of natural and experimental rock deformation phenomena (see reviews in Paterson & Wong, 2005; Scholz, 2002). More recently, experimental studies highlighted the influence of pore pressure buildup on the stability of fault at different scales (De Barros et al., 2016; Guglielmi et al., 2015; Scuderi et al., 2017; Ye & Ghassemi, 2018), as well as on the propagation of the rupture (Ougier-Simonin & Zhu, 2013, 2015).

However, the reactivation criterion based on the effective stress law is expected to hold (within a reasonable degree of approximation) only when the entire fault is affected by fluid pressure, that is, if  $p$  is homogeneous. In other words, the criterion 1 is best viewed as a local one, and the onset of large scale fault motion depends on the distribution of fluid pressure, applied stresses, and elastic stress redistribution due to partial slip (De Barros et al., 2016; Guglielmi et al., 2015).

The reactivation of slip and the mode of sliding (either quasi-static or dynamic) produced by fluid pressure perturbations has been studied extensively in theoretical models based on fracture mechanics (Galis et al., 2017; Garagash & Germanovich, 2012; Viesca & Rice, 2012). These approaches show that local fluid overpressures (i.e.,  $p$  locally greater than expected from a homogeneous Coulomb criterion) can lead to periods of quasi-static, partial fault slip, followed by earthquake nucleation and propagation well beyond the initial pressurized area. Such predictions are in qualitative agreement with field observations showing induced seismicity and fault reactivation in crystalline basements, far from the injection sites (e.g., Keranen et al., 2013). However, theoretical models are necessarily based on simplified assumptions regarding friction laws and do not systematically account for potential couplings between fluid pressure, hydraulic and mechanical properties of rocks, and fault interfaces. The reactivation of faults by fluid pressure variations is expected to be complicated by these coupled hydromechanical processes, and accurate predictions at field scale require an in-depth knowledge of the key controlling fault zone properties and injection parameters.

Here we investigate the conditions for and the characteristics of fault reactivation due to fluid injection in controlled laboratory experiments. We specifically test how the injection rate and background stress conditions influence the onset of fault reactivation. We performed injection tests on saw cut Westerly granite samples subjected to triaxial stress conditions and monitored contemporaneously the evolution of fault slip, stress, and elastic wave velocities across the fault. This setup allowed us to analyze in situ the effect of fluid pressure diffusion on fault reactivation under realistic upper crustal conditions in a major crystalline basement rock type.

## 2. Experimental Setup and Methods

A cylindrical sample of Westerly granite of 40 mm in diameter was cored and then cut and precisely ground to a length of 100 mm. The cylinder was then cut at an angle of 30° with respect to its axis of revolution to create an elliptical saw cut fault interface (Figure 1a) of 40 mm in width and 80 mm in length along strike. The fault surface was prepared with a surface grinder. A 4-mm diameter borehole, the center of which was located at 4.5 mm from the edge of the cylinder, was drilled through the material on one side of the fault, connecting the fault surface to the bottom end of the sample (Figure 1a). The off-center location of the injection borehole was chosen to maximize the fluid diffusion distance along the fault.

The faulted sample was placed in a viton jacket and equipped with 14 piezoelectric transducers arranged in an array shown schematically in Figure 1a. Each transducer consists in an aluminium casing that embeds a 1 mm thick, 5-mm diameter piezoelectric ceramic disk (material reference Plc255 from Physik Instrumente GmbH) that is polarized perpendicular to the sample surface. Five pairs of transducers were positioned along the cylinder in the plane perpendicular to fault strike. This two-dimensional array allowed us to monitor wave velocity variations along 25 raypaths intersecting the fault at a range of locations. Two additional pairs of transducers were placed at the top and bottom of the sample at 90° to the main array.

The instrumented sample was placed in the 400-MPa triaxial oil-medium apparatus of the Rock and Ice Physics Laboratory at University College of London (Eccles et al., 2005). The bottom end of the sample, where the

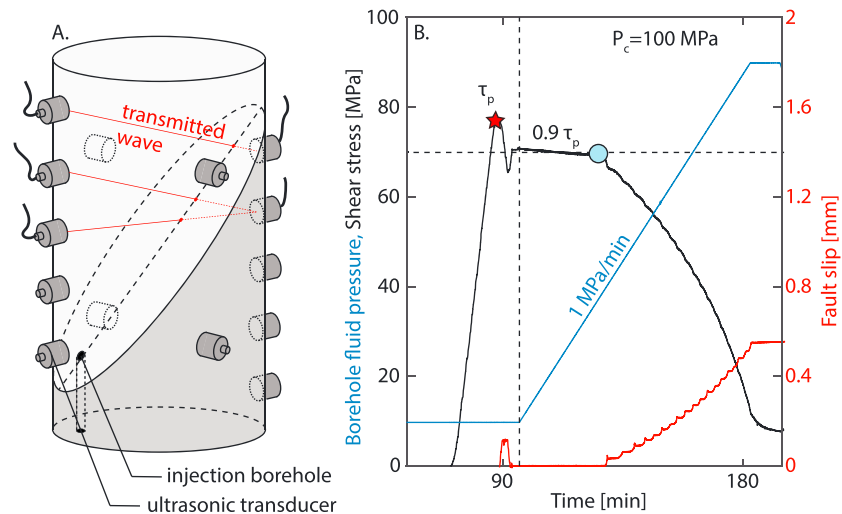


**Figure 1.** Experimental setup. (a) Schematic of the sample assembly. The length of the fault is 8 cm along strike. Injection is conducted in the bottom sample through a borehole reaching the fault surface. (b) Fluid pressure, shear stress, and slip measured during a sliding test at constant pressure (left of dotted vertical line) and during a fluid injection test at 1 MPa/min and initial shear stress equal to 90% of the static frictional strength.

borehole is located, was connected to a high-capacity servo-hydraulic pore fluid intensifier instrumented with a pressure transducer and an linear variable differential transducer that measures the variations of the intensifier fluid volume. The top part of the sample was connected to a closed reservoir instrumented with a separate pressure transducer. The pore fluid used in this study was distilled water. The confining pressure ( $P_c$ ) and the axial differential stress ( $Q$ ) were controlled independently by an electromechanical pump and a servo-hydraulic actuator, respectively. Sample shortening was calculated from an external measurement of the ram displacement, corrected for stiffness of the loading column. Axial load was measured using an external load cell and corrected for seal friction. The differential stress on the sample was computed as the ratio of corrected load over sample cross-sectional area. Fault slip was computed by projecting the sample axial shortening onto the fault direction. The average fault normal and shear stresses were obtained by resolving the triaxial stress state onto the fault plane (Jaeger et al., 2009).

During experiments, ultrasonic wave velocities were measured repeatedly in the following manner. An elastic wave was generated at a known origin time by imposing a high-voltage ( $\sim 250$  V), high-frequency (1 MHz) electric pulse on a given piezoelectric transducer, and the resulting signals were amplified and recorded (at a 50-MHz sampling frequency) on the 13 remaining sensors. This procedure was repeated sequentially so that all transducers are used as active sources, thus generating a total  $14 \times 13$  waveforms (hereafter called a “survey”). During postprocessing, a reference survey is chosen and arrival times of ballistic  $P$  waves are picked manually on all available waveforms. A cross-correlation procedure is employed to determine accurate relative variations in arrival times relative to the reference survey (see details in Brantut, 2015). The relative change in wave velocity between each pair of sensors is obtained as the ratio of the change in arrival time over the reference arrival time, and we also correct from the change in relative position of the sensors as the fault slides.

We conducted experiments at two confining pressures, 50 and 100 MPa. The initial pore pressure was set to 10 MPa. The shear stress at the onset of fault slip under constant pore pressure conditions, denoted  $\tau_p$ , was determined by conducting an axial loading test. Subsequently, the load was decreased down to a given initial stress  $\tau_0$ , and the actuator position was maintained constant by a servo-controlled loop on the external displacement transducers. This situation corresponds to a “stress relaxation” test (Rutter et al., 1978; Rutter & Hackston, 2017; Ye & Ghassemi, 2018) whereby a finite amount of elastic strain energy is stored in the loading column. The onset of fault reactivation induces the release of the strain accumulated in the column by shortening of the sample (here slip on the fault). Fault slip is accompanied by a decrease in the applied stress, in a constant proportion of the sample shortening determined by the machine stiffness. This method ensured that fault slip could not runaway beyond a controlled quantity function of the initial strain energy stored in the medium, while not precluding in principle the occurrence of stick-slip events. Fluid was then injected through the borehole at a constant pressure rate (from 1 to 1,000 MPa/min, measured at the outlet of the pore

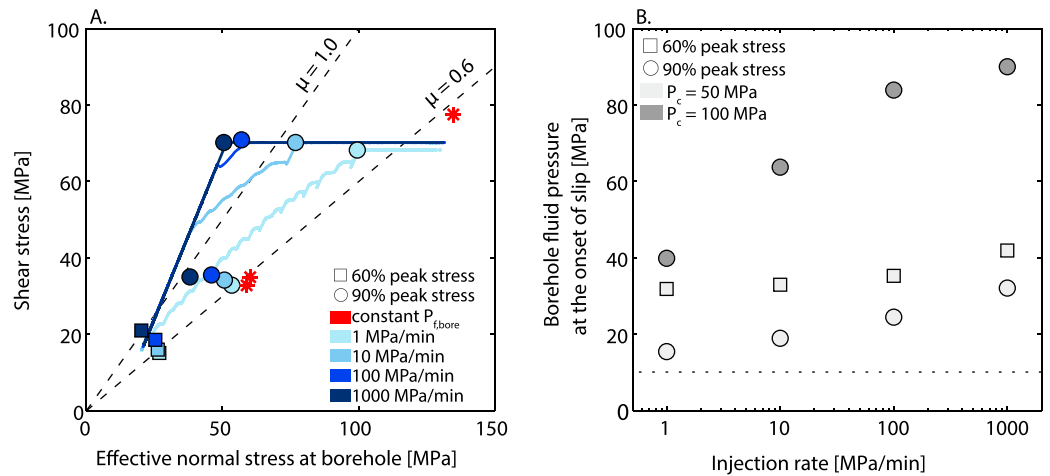


**Figure 2.** Static reactivation of the experimental fault. (a) Mohr diagram presenting the fault reactivation conditions in all experiments. Solid lines correspond to the tracks of the stresses obtained during the experiment conducted at 100-MPa confining pressure and initial stress equal to 90% of  $\tau_p$ . Dashed lines correspond to frictional strength using friction coefficients of 0.6 and 1. Symbols correspond to the state of stress at the onset of slip for each experiments and conditions tested. Red stars: onset of slip under constant pressure conditions. Squares: onset of slip during injection at an initial stress equal to 60% of  $\tau_p$ . Circles: onset of slip during injection at an initial stress equal to 90% of  $\tau_p$ . (b) Fluid pressure allowing fault reactivation as a function of the injection rate. The dashed line corresponds to the background level of the fluid pressure in our experiments.

fluid intensifier), up to a target value of 40 and 90 MPa at  $P_c = 50$  MPa and  $P_c = 100$  MPa, respectively. The permeability of Westerly granite is expected to increase from  $10^{-22}$  to  $10^{-20}$  in the range of effective confining pressure tested (from 90- to 10-MPa effective confining pressure; ; Nasseri et al., 2009; Rutter & Hackston, 2017). During injection, ultrasonic surveys were performed at  $\sim 10$ -s time intervals, and other mechanical data were recorded at  $\sim 5$  Hz.

### 3. Mechanical Results

A representative example of shear stress, borehole fluid pressure, and slip evolution is shown in Figure 1b, for a test conducted at  $P_c = 100$  MPa. During the first stage, the onset of fault slip was measured at  $\tau_p = 78$  MPa. The stress was then decreased to  $\approx 0.9 \times \tau_p$ , and fluid injection was conducted at a rate of 1 MPa/min. The initiation of fault slip was detected at a borehole fluid pressure of  $P_{f,bore} \approx 40$  MPa. With further fluid pressure increase, fault slip continues in a series of steps of  $\sim 20$   $\mu\text{m}$  in amplitude and  $\sim 30$  s in duration, separated by dwell times of the order of 200 s. A similar behaviour is observed in all tests.

The complete stress paths of injection tests performed at  $P_c = 100$  MPa are shown in Figure 2a in effective normal stress (considering the borehole fluid pressure  $P_{f,bore}$ ) versus shear stress space. The onset of fault slip is also marked for all experiments. Fluid injection leads to a decrease of effective normal stress at the borehole without change in the background shear stress. Once the state of stress reaches a critical point (cf. squares and circles), slip initiates and the values of both shear stress and effective normal stress decline progressively. In the tests conducted under the lowest stress conditions ( $P_c = 50$  MPa and  $\tau_0 = 0.6\tau_p$ ) and for injection rates up to 100 MPa/min, the onset of fault slip occurs at an effective normal stress comparable to that expected from a static friction criterion with  $\mu \approx 0.7$ , compatible with the static friction of  $\mu = 0.6$  observed in the test at constant fluid pressure. At 1,000-MPa/min injection rate, the fault reactivates at a slightly lower effective normal stress (as measured at the borehole). When the initial stress  $\tau_0$  is around 90% of  $\tau_p$ , the effective normal stress required to activate fault slip is generally higher than for low initial stresses. At 1 MPa/min, the fault is reactivated at  $P_{f,bore} = 15.5$  MPa, consistent with the measured static friction. However, with increasing injection rate, the effective normal stress at reactivation decreases significantly. The same trend is observed in the tests performed at  $P_c = 100$  MPa.

The borehole fluid pressure required to reactivate the fault is plotted as a function of injection rate in Figure 2b. For all the tests conducted at elevated initial stress, a clear trend toward high fluid pressure at reactivation is observed as the injection rate increases. This trend is clearest at  $P_c = 100$  MPa, where an increase in injection

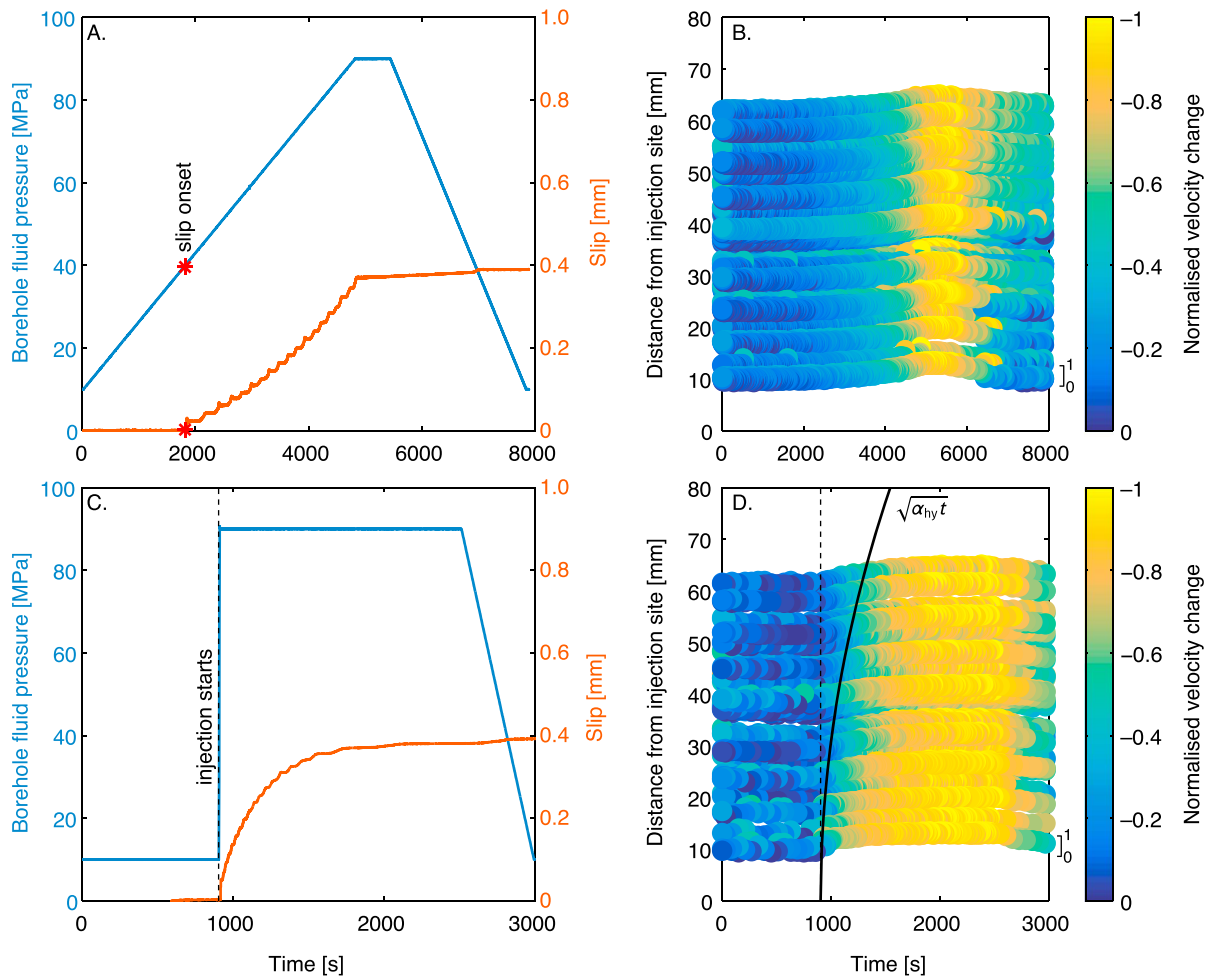


**Figure 3.** Fluid pressure and wave velocities during injection. (a) Evolution of fluid pressure and slip during injection conducted at 1 MPa/min,  $P_c = 100$  MPa. (b) Time evolution of the normalized change in compressional wave velocity during injection conducted at 1 MPa/min,  $P_c = 100$  MPa, as a function of distance between injection point and intersection point of raypath and fault plane. The velocity along each path is normalized by the difference between its extrema. Both vertical variation and color bar correspond to the normalized velocity change. (c and d) Similar to (a) and (b) for an injection conducted at 1,000 MPa/min.

rate from 10 to 100 MPa/min produces an increase in fluid pressure at reactivation from around 64 to 84 MPa. At the highest injection rate (1,000 MPa/min), the target pressure of 90 MPa was reached and slip initiated 4.8 s after that point. The stress paths (as measured at the borehole) shown in Figure 2a are significantly above the static friction criterion, especially at high injection rate.

#### 4. Wave Velocity Variations

Our experimental results suggest that at low injection rate and low stress, the onset of fault reactivation follows a regular Coulomb criterion. However, increasing the injection rate trends to modify the reactivation criterion of the same experimental fault. This behavior is enhanced by increasing the state of stress acting on the fault plane prior the injection.

To understand this change in the onset of fault reactivation with increasing injection rate, we use elastic wave speed measurements as a proxy to track the evolution of the fluid pressure along the fault. Increasing the fluid pressure under constant confining pressure conditions is expected to decrease the elastic wave speed of the fault system as a response to (i) microcracks opening due to the decrease of the effective pressure in the bulk material (Nasseri et al., 2009; Walsh, 1965) and (ii) the decrease of the contact stiffness of the experimental fault (Guéguen & Kachanov, 2011; Kelly et al., 2017). The evolution of compressional wave velocities across the fault during injections conducted at 1 and 1,000 MPa/min and 100 MPa confining pressure are presented in Figure 3.

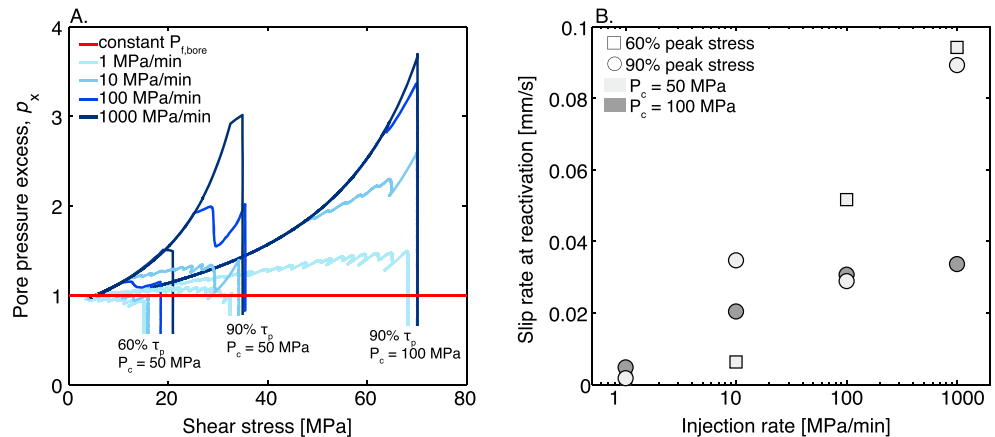


**Figure 4.** Fluid overpressure and slip rate during reactivation. (a) Evolution of the pore pressure excess factor (equation (2)) during each fluid injection. (b) Slip rate at the onset of slip as a function of the injection rate.

During the injection conducted at 1 MPa/min (Figures 3a and 3b), the wave velocity along each raypath decreases progressively with increasing fluid pressure, down to a maximum drop of the order of 2–3% at the maximum fluid pressure of 90 MPa (10-MPa effective confining pressure). At this injection rate, the velocity evolves homogeneously independently of the distance from the injection site, which suggests that fluid pressure is relatively homogeneous along the fault throughout the injection process.

At high injection rate (1,000 MPa/min; Figures 3c and 3d), the drop in velocity is a function of the distance from the injection site. At early stage, when the fluid pressure has reached its maximum of 90 MPa and fault slip initiates, a sharp drop in velocity is observed along the raypaths crossing the fault nearest to the injection site, while no change is observed along raypaths intersecting the fault at distances larger than 3 cm from the injection site. Far from the injection point, the velocity change is gradual and reaches its maximum  $\sim 500$  s after injection starts. Considering that the changes in wave velocities observed along the fault are mostly due to the propagation of a fluid pressure front during fluid injection, we compute an estimate of the location of the diffusive pressure front as  $\sqrt{\alpha_{hy}t}$ , where  $\alpha_{hy}$  is the hydraulic diffusivity of the fault and  $t$  is the time from the beginning of injection. Using  $\alpha_{hy} = 10^{-5} \text{ m}^2\text{s}^{-1}$ , the time at which 80% of the maximum drop in wave velocity is observed along each raypath is acceptably matched by the characteristic diffusion time from the pressurized borehole (see black line in Figure 3d).

## 5. Influence of Background Stress Level and Injection Rate on Fluid Pressure Heterogeneity

Our experimental results indicate that while fluid pressure remains homogeneous over the fault during experiments conducted at low injection rate, a fluid pressure front is observed at high injection rate. This suggests that increasing the fluid injection rate leads to an increase of the fluid pressure heterogeneity over the fault plane. Note that the background stress prior injection, as the confining pressure acting on the fault system, seems to enhance this heterogeneity, that is, the intensity of fluid overpressure leading to instability (Figures 2a). To analyze these processes further, we follow Rutter and Hackston (2017) and compute a pore pressure excess factor defined as

$$p_x = \frac{P_{f,bore}}{\sigma_n - \tau/\mu} \quad (2)$$

where  $\mu = 0.6$  is the static friction coefficient of the fault. A local fluid overpressure is required to reactivate the fault if  $p_x$  becomes greater than 1 during the fluid injection history, whereas  $p_x = 1$  if the effective stress principle applies. The evolution of  $p_x$  as a function of the shear stress during each injection is presented in Figure 4. During the tests conducted at  $P_c = 50$  MPa and  $\tau_0 = 0.6\tau_p$ , the fault generally reactivates following  $p_x \approx 1$ . Only the injection conducted at the highest rate (1,000 MPa/min) highlights fluid overpressure, with a pore fluid excess factor of around 1.4 at the onset of fault reactivation (Figure 4). By contrast, at elevated background stress and confining pressure ( $P_c = 100$  MPa,  $\tau_0 = 0.9\tau_p$ ),  $p_x$  increases significantly with increasing

injection rate, from 1.5 to 3.7 as injection rate increases from 1 to 1,000 MPa/min. Overall, increases in either confining pressure or initial shear stress lead to an increase of the local fluid pressure required for fault reactivation. Beyond the onset of slip, the fault offloads due to the progressive relaxation of the loading column as slip proceeds, and the amount of required fluid overpressure decreases. This observation is similar to that of Rutter and Hackston (2017) during fluid pressurization of faults with low hydraulic conductivity.

## 6. Discussion and Conclusions

Our results show unambiguously that both stress state and injection rate modify the conditions for fault reactivation. At elevated stress and during fast, *local* fluid injection, our wave velocity measurements indicate that fluid pressure is heterogeneous along the fault, which explains why a conventional Coulomb law combined with a simple effective stress law is not an appropriate reactivation criterion. In other words, we observe a transition from a homogeneous case, where a static empirical friction law applies (within typical uncertainties), to a heterogeneous case, where the onset of sliding is best viewed as a (nonlocal) fracture problem and controlled by local stress concentrations along the fault plane (e.g., Rubinstein et al., 2004; Svetlizky & Fineberg, 2014).

The degree of heterogeneity in pore fluid pressure along the fault is controlled by the balance between the hydraulic diffusion rate and injection rate. The hydraulic properties of the fault and surrounding rock are thus key parameters controlling the extent to which fault reactivation deviates from Coulomb's law. At a given injection rate, our results show that an increase of the confining pressure and/or initial shear stress enhances the fluid pressure required at the injection site for fault reactivation, as well as the fluid pressure heterogeneity along the fault. This observation is explained by the fact that increasing fault normal and shear stresses tend to reduce fault hydraulic transmissivity (e.g., Rutter & Hackston, 2017), and overall increases in mean stress reduce bulk rock permeability (e.g., Nasser et al., 2009). This decrease in hydraulic transmissivity slows fluid diffusion along the fault, and promotes the transition from "drained" to "locally undrained" conditions. In the former case, only a small fluid pressure gradient is formed during injection and fluid pressure remains almost homogeneous along the fault, whereas in the latter case a strong fluid pressure gradient is formed within the finite length of our experimental fault. The transition between these two regimes is expected to occur when the hydraulic diffusion length  $L_{\text{diff}}$  becomes smaller than the length of the fault  $L_f$ . The diffusion length is given as  $L_{\text{diff}} = \sqrt{\alpha_{\text{hy}} t_c}$ , where  $t_c$  is the characteristic time of pressurization. A natural estimate of  $t_c$  in our experiments is given by the product  $t_c = 1/(\dot{P}S)$ , where  $\dot{P}$  is the pressurization rate and  $S$  the storativity of the fault. Therefore, the transition from drained to locally undrained conditions occurs when the imposed fluid pressure injection rate  $\dot{P}$  becomes greater than a critical fluid pressure injection rate defined as  $\dot{P}_{\text{crit}} = \alpha_{\text{hy}}/(L_f^2 S)$ . Assuming a storage capacity of the fault  $S$  of the order of  $10^{-10}$  Pa $^{-1}$  and using a hydraulic diffusivity of  $10^{-5}$  m $^2$ /s, we find that  $\dot{P}_{\text{crit}}$  is of the order of 1 GPa/min, which is consistent with our observation of a diffusion front in the test conducted at the highest injection rates. The critical pressurization rate  $\dot{P}_{\text{crit}}$  can be rewritten as a function of the permeability of the fault  $k$  and the viscosity of the fluid injected  $\eta$  following  $\dot{P}_{\text{crit}} = k/(\eta S^2 L_f^2)$ . This relation highlights that the transition from drained to locally undrained conditions is enhanced by increasing the viscosity of the fluid injected (relevant for hydraulic fracturing) and by the length of the fault, as well as by lowering the permeability of the fault system.

In our experiments, the onset of fault reactivation is observable only when the entire fault is able to slip, that is, when the slipping patch reaches the sample's edge. Our experimental results suggest that drained and locally undrained conditions lead to two distinct reactivation scenarios. In the drained case, the slip patch grows behind the fluid pressure front, similarly to previous experimental results obtained at a larger scale (Guglielmi et al., 2015): fault reactivation follows a conventional Coulomb law combined with a simple effective stress law. In the locally undrained case, the fault reactivates when only a small fraction of the fault is at elevated fluid pressure. This local increase of fluid pressure induces the propagation of a slip front which largely outgrows the pressurized region. These results are qualitatively consistent with the theoretical analysis developed by Garagash and Germanovich (2012), whereby a localized fluid pressure increase on a critically loaded fault (here when  $\tau_p - \tau_0 \ll \mu(P_{f,\text{bore}} - P_{f,0})$ , where  $P_{f,0}$  is the initial homogeneous fluid pressure) acts as a point force. In that case, the local pore pressure required to propagate slip is larger than the one expected from Coulomb criterion, and the slipping patch largely outgrows the original pressurized region. Our experiments provide direct evidence for this phenomenon, notably at the highest injection rate where the entire experimental fault is sliding while the fluid pressure front remains localized near the borehole (Figure 3d).

In the locally undrained scenario, the velocity of the expanding slip patch is expected to be linked to the injection rate (e.g., Dublanchet & Viesca, 2017; Garagash & Germanovich, 2012). While the experimental configuration did not allow to capture the propagation of the slip front, our measurements show that the slip rate at the onset of reactivation increases with the injection rate for each stress conditions tested (Figure 4b). These results suggest that the intensity of the local fluid pressure perturbation enhances the slip rate and stress transfer at the onset of fault reactivation. Inasmuch as seismogenic fault exhibits generally velocity-weakening behavior, an increase in the injection rate is expected to enhance the nucleation of instabilities, all the more so than transiently high slip rates can trigger strongly rate-weakening mechanisms that facilitate dynamic rupture propagation. Depending on the fault stress state at large distances from the injection point, slip instabilities can naturally arrest (under low stress conditions) or grow and become large earthquakes (at high stress; e.g., ; Garagash & Germanovich, 2012; Viesca & Rice, 2012).

The hydraulic diffusivity of the fault and surrounding material is expected to increase during slip due to progressive unloading and average decrease of the effective pressure, accelerating the homogenisation of the fluid pressure, as observed in our experiments. This phenomenon is potentially complexified by slip-induced dilatancy, inducing variations in along-fault hydraulic diffusivity. In addition, wear processes, gouge formation, and grain crushing are expected to induce a decrease in fault permeability (e.g., Olsson & Brown, 1993; Rutter & Hackston, 2017; Zhang & Tullis, 1998), which might reduce the ability of the fluid pressure front to reach regions far from the injection point (where slip is concentrated; see Garagash & Germanovich, 2012).

Note that in none of our experiments were dynamic stress drops observed during off-loading, although episodes of relatively rapid but stable sliding were seen. This aseismic behavior is imposed by the stiffness of the apparatus compared to the stiffness of the experimental fault (e.g., Leeman et al., 2016), and by our experimental procedure, that is, stress relaxation experiments. In our experimental setup, the dimension of the fault (and its effective compliance) is too small to observe fully developed dynamic runaway ruptures. Faster ruptures might be observable by artificially increasing the compliance of the fault and apparatus system, by imposing a constant applied stress with a servo-controlled load—a rather risky procedure in terms of safety and integrity of the deformation apparatus. However, injection-induced fracture experiments in sandstone indicate that ruptures might be inherently more stable when triggered by fluid pressure increases compared to shear stress increases (e.g., French et al., 2016; Ougier-Simonin & Zhu, 2013; 2015). However, further analysis is required to determine whether such an effect is intrinsic to fluid pressurization or whether it results from the combination of experimental conditions (e.g., apparatus stiffness) and rock types used.

Taken together, the experimental results presented here emphasize that hydromechanical coupling processes, notably the dependence of transport properties on stress state, have a key control on fault reactivation by localized fluid injection, consistent with theoretical models (e.g., Cappa & Rutqvist, 2011) and field observations (e.g., Guglielmi et al., 2015). In nature, measurements of *in situ* stress states in the upper crust have shown that the shear stress is close to the static strength limit for brittle failure (e.g., Townend & Zoback, 2000). Initial natural stress conditions and fault properties are therefore expected to promote locally undrained conditions at the scale of the reservoir and, based on this study, promote the development of fluid pressure heterogeneities along faults during fluid injection. In addition, fluid injection sites are rarely directly into the cores of fault zones, but rather at a distance from the fault system, which could also promote heterogeneity of the fluid pressure along faults and complex poroelasticity response of the system. Our experimental results confirm theoretical analyses (e.g., Dublanchet & Viesca, 2017; Garagash & Germanovich, 2012) showing that these local fluid pressure heterogeneities initiate the propagation of local slip fronts and induce stress transfer far away from the injection site. The development of such heterogeneities, superimposed with possible pre-existing fault structures and background stress profiles, makes accurate predictions of threshold pressure (or injected volume) for fault reactivation and rupture propagation difficult. The time-dependent nature of both fluid flow and fault friction also implies that delayed reactivation is possible (as observed in one of our tests), and changes and spatial variations in fault permeability influence the location and timing of induced seismicity (e.g., Chang & Segall, 2016; Vlček et al., 2018; Yeck et al., 2016), supporting the continuation of seismicity following the end of injection reported in oil and gas related reservoirs (Ogwari et al., 2018). This implies that in nature, slowing down or stopping fluid injection does not necessarily hamper further fault reactivation, especially as fluids (and fluid pressure) might accumulate along low permeability barriers (e.g., Passelègue et al., 2014; Yehya et al., 2018).

### Acknowledgments

F. X. P. acknowledges funding provided by the Swiss National Science Foundation through grant PZENP2/173613. This work was funded, in part, by the UK Natural Environment Research Council through grant NE/K009656/1 to N. B. Discussions with Dmitry Garagash, Robert Viesca, Pierre Dublanquet, and Marie Violay are gratefully acknowledged. We thank A. Fagereng, M. Scuderi, and T. Goebel for their comments, which improved the paper significantly. Experimental data are available from the UK National Geoscience Data Centre (<http://www.bgs.ac.uk/services/ngdc/>) or upon request to the corresponding author.

### References

- Barbour, A. J., Norbeck, J. H., & Rubinstein, J. L. (2017). The effects of varying injection rates in Osage County, Oklahoma, on the 2016 Mw 5.8 Pawnee earthquake. *Seismological Research Letters*, *88*, 1040–1053. <https://doi.org/10.1785/0220170003>
- Brantut, N. (2015). Time-dependent recovery of microcrack damage and seismic wave speeds in deformed limestone. *Journal of Geophysical Research: Solid Earth*, *120*, 8088–8109. <https://doi.org/10.1002/2015JB012324>
- Byerlee, J. (1978). Friction of rocks. *Pure and Applied Geophysics*, *116*, 615–626. <https://doi.org/10.1007/BF00876528>
- Cappa, F., & Rutqvist, J. (2011). Modeling of coupled deformation and permeability evolution during fault reactivation induced by deep underground injection of CO<sub>2</sub>. *International Journal of Greenhouse Gas Control*, *5*(2), 336–346.
- Chang, K., & Segall, P. (2016). Injection-induced seismicity on basement faults including poroelastic stressing. *Journal of Geophysical Research: Solid Earth*, *121*, 2708–2726. <https://doi.org/10.1002/2015JB012561>
- Cornet, F., Helm, J., Poitrenaud, H., & Etchecopar, A. (1997). Seismic and aseismic slips induced by large-scale fluid injections. *Pure and applied geophysics*, *150*(3–4), 563–583.
- De Barros, L., Daniel, G., Guglielmi, Y., Rivet, D., Caron, H., Payre, X., et al. (2016). Fault structure, stress, or pressure control of the seismicity in shale? insights from a controlled experiment of fluid-induced fault reactivation. *Journal of Geophysical Research: Solid Earth*, *121*, 4506–4522. <https://doi.org/10.1002/2015JB012633>
- Dieterich, J. H., Richards-Dinger, K. B., & Kroll, K. A. (2015). Modeling injection-induced seismicity with the physics-based earthquake simulator RSQSim. *Seismological Research Letters*, *86*(4), 1102–1109.
- Dublanquet, P., & Viesca, R. C. (2017). Dynamics of fluid induced aseismic slip. 79th EAGE Conference and Exhibition 2017.
- Eccles, D., Sammonds, P., & Clint, O. (2005). Laboratory studies of electrical potential during rock failure. *International Journal of Rock Mechanics and Mining Sciences*, *42*(7), 933–949.
- Ellsworth, W. L. (2013). Injection-induced earthquakes. *Science*, *341*(6142), 1225–1229.
- French, M. E., Zhu, W., & Banker, J. (2016). Fault slip controlled by stress path and fluid pressurization rate. *Geophysical Research Letters*, *43*, 4330–4339. <https://doi.org/10.1002/2016GL068893>
- Galis, M., Ampuero, J. P., Mai, P. M., & Cappa, F. (2017). Induced seismicity provides insight into why earthquake ruptures stop. *Science Advances*, *3*(12), eaap7528.
- Garagash, D. I., & Germanovich, L. N. (2012). Nucleation and arrest of dynamic slip on a pressurized fault. *Journal of Geophysical Research*, *117*, B10310. <https://doi.org/10.1029/2012JB009209>
- Goebel, T. H., Walter, J. I., Murray, K., & Brodsky, E. E. (2017). Comment on: How will induced seismicity in Oklahoma respond to decreased saltwater injection rates? by C. Langenbruch and MD Zoback. *Science Advances*, *3*(8), e1700441.
- Guéguen, Y., & Kachanov, M. (2011). Effective elastic properties of cracked rocks—An overview. In Y. M. Leroy & F. K. Lehner (Eds.), *Mechanics of Crustal Rocks, CISM Courses and Lectures*, (Vol. 533) Vienna: Springer.
- Guglielmi, Y., Cappa, F., Avouac, J.-P., Henry, P., & Ellsworth, D. (2015). Seismicity triggered by fluid injection—induced aseismic slip. *Science*, *348*(6240), 1224–1226.
- Healy, J., Rubey, W., Griggs, D., & Raleigh, C. (1968). The Denver earthquakes. *Science*, *161*(3848), 1301–1310.
- Jaeger, J. C., Cook, N. G., & Zimmerman, R. (2009). *Fundamentals of rock mechanics*. Oxford, UK: John Wiley & Sons.
- Kelly, C., Faulkner, D., & Rietbrock, A. (2017). Seismically invisible fault zones: Laboratory insights into imaging faults in anisotropic rocks. *Geophysical Research Letters*, *44*, 8205–8212. <https://doi.org/10.1002/2017GL073726>
- Keranen, K. M., Savage, H. M., Abers, G. A., & Cochran, E. S. (2013). Potentially induced earthquakes in Oklahoma, USA: Links between wastewater injection and the 2011 Mw 5.7 earthquake sequence. *Geology*, *41*(6), 699–702.
- Langenbruch, C., & Zoback, M. D. (2016). How will induced seismicity in Oklahoma respond to decreased saltwater injection rates? *Science Advances*, *2*(11), e1601542.
- Leeman, J., Saffer, D., Scuderi, M., & Marone, C. (2016). Laboratory observations of slow earthquakes and the spectrum of tectonic fault slip modes. *Nature Communications*, *7*, 11104.
- Nasser, M., Schubnel, A., Benson, P., & Young, R. (2009). Common evolution of mechanical and transport properties in thermally cracked westerly granite at elevated hydrostatic pressure. *Pure and Applied Geophysics*, *166*(5–7), 927–948.
- Ogware, P. O., DeShon, H. R., & Hornbach, M. J. (2018). The Dallas-Fort Worth airport earthquake sequence: Seismicity beyond injection period. *Journal of Geophysical Research: Solid Earth*, *123*, 553–563. <https://doi.org/10.1002/2017jb015003>
- Olsson, W., & Brown, S. (1993). Hydromechanical response of a fracture undergoing compression and shear. *International journal of rock mechanics and mining sciences & geomechanics abstracts* (Vol. 30, pp. 845–851). B.V: Elsevier.
- Ougier-Simonin, A., & Zhu, W. (2013). Effects of pore fluid pressure on slip behaviors: An experimental study. *Geophysical Research Letters*, *40*, 2619–2624. <https://doi.org/10.1002/grl.50543>
- Ougier-Simonin, A., & Zhu, W. (2015). Effect of pore pressure buildup on slowness of rupture propagation. *Journal of Geophysical Research: Solid Earth*, *120*, 7966–7985. <https://doi.org/10.1002/2015JB012047>
- Passelègue, F. X., Fabbri, O., Dubois, M., & Ventalon, S. (2014). Fluid overpressure along an oligocene out-of-sequence thrust in the shimanto belt, SW Japan. *Journal of Asian Earth Sciences*, *86*, 12–24.
- Paterson, M. S., & Wong, T.-f. (2005). *Experimental rock deformation—The brittle field*. Berlin/Heidelberg, Germany: Springer Science & Business Media.
- Raleigh, C., Healy, J., & Bredehoeft, J. (1976). An experiment in earthquake control at Rangely, Colorado. *work (Fig. 1b)*, *108*(52), 30.
- Rubinstein, S. M., Cohen, G., & Fineberg, J. (2004). Detachment fronts and the onset of dynamic friction. *Nature*, *430*(7003), 1005.
- Rubinstein, J. L., Ellsworth, W. L., McGarr, A., & Benz, H. M. (2014). The 2001–present induced earthquake sequence in the Raton basin of northern New Mexico and Southern Colorado. *Bulletin of the Seismological Society of America*, *104*, 2162–2181.
- Rutter, E., Atkinson, B., & Mainprice, D. (1978). On the use of the stress relaxation testing method in studies of the mechanical behaviour of geological materials. *Geophysical Journal International*, *55*(1), 155–170.
- Rutter, E., & Hackston, A. (2017). On the effective stress law for rock-on-rock frictional sliding, and fault slip triggered by means of fluid injection. *Philosophical Transactions of the Royal Society A*, *375*(2103), 20160001.
- Scholz, C. H. (2002). *The Mechanics of Earthquakes and Faulting*. Cambridge, UK: Cambridge University Press.
- Scuderi, M., Collettini, C., & Marone, C. (2017). Frictional stability and earthquake triggering during fluid pressure stimulation of an experimental fault. *Earth and Planetary Science Letters*, *477*, 84–96.
- Sibson, R. H. (1985). A note on fault reactivation. *Journal of Structural Geology*, *7*(6), 751–754.
- Svetlizky, I., & Fineberg, F. (2014). Classical shear cracks drive the onset of dry frictional motion. *Nature*, *509*(7499), 205–208.
- Townend, J., & Zoback, M. D. (2000). How faulting keeps the crust strong. *Geology*, *28*(5), 399–402.
- Viesca, R. C., & Rice, J. R. (2012). Nucleation of slip-weakening rupture instability in landslides by localized increase of pore pressure. *Journal of Geophysical Research*, *117*, B03104. <https://doi.org/10.1029/2011JB008866>

- Vlček, J., Eisner, L., Stabile, T. A., & Telesca, L. (2018). Temporal relationship between injection rates and induced seismicity. *Pure and Applied Geophysics*, *175*(8), 2821–2835.
- Walsh, J. (1965). The effect of cracks on the uniaxial elastic compression of rocks. *Journal of Geophysical Research*, *70*(2), 399–411.
- Warpinski, N., & Teufel, L. (1987). Influence of geologic discontinuities on hydraulic fracture propagation (includes associated papers 17011 and 17074). *Journal of Petroleum Technology*, *39*(02), 209–220.
- Ye, Z., & Ghassemi, A. (2018). Injection-induced shear slip and permeability enhancement in granite fractures. *Journal of Geophysical Research: Solid Earth*, *123*, 9009–9032. <https://doi.org/10.1029/2018JB016045>
- Yeck, W., Weingarten, M., Benz, H. M., McNamara, D. E., Bergman, E., Herrmann, R., et al. (2016). Far-field pressurization likely caused one of the largest injection induced earthquakes by reactivating a large preexisting basement fault structure. *Geophysical Research Letters*, *43*, 10,198–10,207. <https://doi.org/10.1002/2016GL070861>
- Yehya, A., Yang, Z., & Rice, J. R. (2018). Effect of fault architecture and permeability evolution on response to fluid injection. *Journal of Geophysical Research: Solid Earth*, *123*. <https://doi.org/10.1029/2018JB016550>
- Zhang, S., & Tullis, T. E. (1998). The effect of fault slip on permeability and permeability anisotropy in quartz gouge. *Tectonophysics*, *295*(1-2), 41–52.
- Zoback, M. D., & Harjes, H.-P. (1997). Injection-induced earthquakes and crustal stress at 9 km depth at the KTB deep drilling site, Germany. *Journal of Geophysical Research*, *102*(B8), 18,477–18,491.